

Weakened Magnetic Braking Signals the Collapse of the Global Stellar Dynamo

TRAVIS S. METCALFE,¹ JENNIFER L. VAN SADERS,² MARC H. PINSONNEAULT,³ THOMAS R. AYRES,⁴ OLEG KOCHUKHOV,⁵
KEIVAN G. STASSUN,⁶ ADAM J. FINLEY,⁷ VICTOR SEE,⁸ ILYA V. ILYIN,⁹ AND KLAUS G. STRASSMEIER⁹

¹Center for Solar-Stellar Connections, White Dwarf Research Corporation, 9020 Brumm Trail, Golden, CO 80403, USA

²Institute for Astronomy, University of Hawai'i, 2680 Woodlawn Drive, Honolulu, HI 96822, USA

³Department of Astronomy, The Ohio State University, 140 West 18th Avenue, Columbus, OH 43210, USA

⁴Center for Astrophysics and Space Astronomy, 389 UCB, University of Colorado, Boulder, CO 80309, USA

⁵Department of Physics and Astronomy, Uppsala University, Box 516, SE-75120 Uppsala, Sweden

⁶Vanderbilt University, Department of Physics & Astronomy, 6301 Stevenson Center Lane, Nashville, TN 37235, USA

⁷Université Paris-Saclay, Université Paris Cité, CEA, CNRS, AIM, F-91191, Gif-sur-Yvette, France

⁸School of Physics & Astronomy, University of Birmingham, Edgbaston, Birmingham B15 2TT, UK

⁹Leibniz-Institut für Astrophysik Potsdam (AIP), An der Sternwarte 16, D-14482 Potsdam, Germany

ABSTRACT

Weakened magnetic braking (WMB) was originally proposed in 2016 to explain anomalously rapid rotation in old field stars observed by the Kepler mission. The proximate cause was suggested to be a transition in magnetic morphology from larger to smaller spatial scales. In a series of papers over the past five years, we have collected spectropolarimetric measurements to constrain the large-scale magnetic fields for a sample of stars spanning this transition, including a range of spectral types from late F to early K. During this time, we gradually improved our methods for estimating the wind braking torque in each of our targets, and for evaluating the associated uncertainties. Here, we reanalyze the entire sample with a focus on uniformity for the relevant observational inputs. We supplement the sample with two additional active stars to provide more context for the evolution of wind braking torque with stellar Rossby number (Ro). The results demonstrate unambiguously that standard spin-down models can reproduce the evolution of wind braking torque for active stars, but WMB is required to explain the subsequent abrupt decrease in torque as Ro approaches a critical value for dynamo excitation. This transition is seen in both the large-scale magnetic field and the X-ray luminosity, indicating weakened coronal heating. We interpret these transitions as evidence of a rotational threshold for the influence of Coriolis forces on global convective patterns and the resulting inefficiency of the global stellar dynamo.

1. INTRODUCTION

In astronomy we are fond of dividing stars into classes. Some categories are even useful, and the broad principles behind them are tied to fundamental astrophysics. Rotation, and its time evolution, is one such case. One of the most fundamental divisions in stellar astrophysics—between high and low mass stars—is clearly seen in the evolution of their rotation rates (e.g., see Kraft 1967, their Fig.1). The median high mass star rotates much faster than the median low mass star. High mass stars, as a rule, do not spin down due to magnetized winds. Low mass stars do. Exceptions to these rules are important, because they test our assumptions and lead to deeper physical understanding. This paper is about weakened magnetic braking (WMB) in low mass stars, and its consequences for the origin and evolution of stellar magnetism, and for rotation as an age diagnostic.

The standard model of stellar spin-down is a natural starting point because magnetized winds are efficient engines for angular momentum loss. The physical model is straightforward:

the wind co-rotates with the star to a characteristic Alfvén radius, which is much larger than the radius of the star. Weber & Davis (1967) demonstrated that the solar wind could remove enough angular momentum to explain the slow solar rotation. However, extrapolating beyond the Sun was difficult. Both of the key ingredients—the large-scale magnetic field strength and the mass-loss rate—are extremely difficult to measure in other stars, and this was even more true in the 1960s than it is today. The next key development in the field was the careful collation of empirical data by Skumanich (1972). He demonstrated that activity diagnostics, the surface lithium abundance, and the rotation rate of stars all scale with age as $t^{-1/2}$. Lithium appears here because it can be destroyed by rotationally induced mixing (Pinsonneault 1997), and the destruction rate is expected to be proportional to the rotation rate. When coupled with the Weber-Davis model, the Skumanich relations can be explained if the magnetic field strength is proportional to the rotation rate.

By the 1990s there was a wave of new data. Efficient spectrographs with CCDs could measure rotational line broadening, which uncovered a population of young cluster stars with a wide range of rotation rates (Soderblom et al. 1983; Stauffer & Hartmann 1987). Time domain surveys yielded rotation periods from spot modulation, beginning with the pioneering Mount Wilson survey (Baliunas et al. 1996) and continuing to studies of rotation in open clusters, such as the Hyades (Radick et al. 1987). X-ray data from ROSAT and ultraviolet data from IUE added a wealth of knowledge about coronal and chromospheric activity. This was complemented by the development of theoretical models for angular momentum evolution (Pinsonneault et al. 1989, 1990). By the end of the 1990s, a coherent model for angular momentum evolution had been developed (Krishnamurthi et al. 1997). The range of initial rotation rates arose from star-disk interactions (Koenigl 1991; Shu et al. 1993). The magnetic field strength increased with rotation rate, as inferred by Skumanich, until it saturated at a critical level (MacGregor & Brenner 1991). A transient phase of core-envelope decoupling, with a timescale of tens of Myr, was needed for solar-type stars (Charbonneau & MacGregor 1993).

Time domain surveys from space then arose, and they utterly transformed stellar astrophysics. The Kepler mission (Borucki et al. 2010) yielded tens of thousands of rotation periods for field stars (McQuillan et al. 2014). Rotation was now a viable chronometer for large stellar samples, giving rise to the field of gyrochronology (Barnes 2007). The limitations of purely solar-scaled models also became apparent. In response, there was a burst of new work on magnetized winds (Matt et al. 2012; Reiners & Mohanty 2012; Gallet & Bouvier 2013; van Saders & Pinsonneault 2013; Garraffo et al. 2018; Spada & Lanzafame 2020). A central insight was the governing role of the Rossby number (Ro), or the ratio between rotation period and convective overturn timescale. In these models, both the magnetic field strength and the mass-loss rates were explicitly tied to Ro , and the results were much more successful at explaining the underlying mass trends. However, the new generation of models all used indirect proxies for the magnetic fields and the mass loss, scaling them relative to global stellar properties.

In stubborn contradiction to theory, stars less active than the Sun failed to slow down at the expected rate (van Saders et al. 2016, 2019). Furthermore, this weakened braking also appeared to be tied to Ro ; it occurs at a shorter rotation period for F stars than for G, and the threshold for K stars is slower still. Motivated by these results, we have engaged in a systematic campaign to bypass activity proxies and more directly measure large-scale magnetic field strengths (Metcalf et al. 2021, 2022, 2023, 2024, 2025). We are also using X-ray measurements, as opposed to abstract scalings with global properties, to infer mass-loss rates. Finally, we have com-

plemented the new data with a new generation of theoretical torque calculations (Finley & Matt 2018).

In this paper we engage in a systematic reanalysis, placing the measurements and models on a common scale. With the new data and modeling, we are now in a position to address several key questions. Is Ro a unique predictor for the onset of weakened braking? Is the transition instantaneous or gradual? To what extent does a change in field morphology, rather than decreasing field strength, matter? Is there evidence for an anomaly in the magnetic field strength, the mass-loss rate, or both? We summarize our uniform sample of stellar properties in Section 2, we describe our homogeneous approach to stellar modeling in Section 3, and we analyze and discuss the results in Section 4.

2. OBSERVATIONS

In our previous work, we adopted stellar properties from a variety of sources in an effort to make the resulting estimates of wind braking torque as reliable as possible. For this paper, we shift the focus to uniformity across the sample to ensure that our inferences of the onset and magnitude of WMB are robust. In this section we describe our adopted sources for global stellar properties (§2.1), as well as our updated approach to constrain the magnetic morphology (§2.2) and the mass-loss rate (§2.3) for each of our targets.

2.1. Stellar Properties

We began by adopting a uniform set of spectroscopic parameters from Valenti & Fischer (2005), including the effective temperature T_{eff} , surface gravity $\log g$, metallicity $[M/H]$, and projected rotational velocity $v \sin i$. All of our targets were included in this catalog, while the more recent catalog of Brewer et al. (2016) contains only a subset.

We used these parameters to obtain empirical constraints on the stellar luminosities and radii from an analysis of the broadband spectral energy distribution (SED) for each star, following the approach described by Stassun & Torres (2016) and Stassun et al. (2017, 2018). This analysis relies on FUV and NUV magnitudes from GALEX, UBV magnitudes from Mermilliod (2006), Strömgren $ubvy$ magnitudes from Paunzen (2015), JHK_S magnitudes from 2MASS, and W1–W4 magnitudes from WISE, in some cases spanning the full stellar SED from 0.2–20 μm . We fit the available data for each target using Kurucz stellar atmosphere models with the adopted spectroscopic parameters and the extinction A_V fixed at zero for these nearby stars. We integrated the resulting model SED to determine the bolometric flux at Earth, and we combined this with the Gaia DR3 parallax (Gaia Collaboration et al. 2021) to calculate the bolometric luminosity L_{bol} . The values of L_{bol} and T_{eff} yield the stellar radius R from the Stefan-Boltzmann relation, while the stellar mass M was derived from the spectroscopic parameters using the eclipsing-binary based empirical relations of Torres et al. (2010).

Table 1. Uniform Stellar Properties for the Magnetic Braking Sample

Star	Name	$ B_d $ (G)	$ B_q $ (G)	$ B_o $ (G)	\dot{M} (\dot{M}_\odot)	P_{rot} (days)	M (M_\odot)	R (R_\odot)	Torque (10^{30} erg)	Ro (Ro_\odot)
Sun	...	1.54	1.07	2.74	1.00	25.4	1.00	1.000	0.351 $^{+0.249}_{-0.151}$	1.000
HD 10476	107 Psc	4.24	2.77	1.37	0.64 $^{+0.76}_{-0.46}$	35 \pm 0.5	0.86 \pm 0.05	0.811 \pm 0.017	0.311 $^{+0.211}_{-0.169}$	0.935 $^{+0.073}_{-0.064}$
HD 10700	τ Cet	0.86 $^{+0.34}_{-0.34}$	0.10 $^{+0.13}_{-0.08}$	34 \pm 0.5	0.82 \pm 0.05	0.836 \pm 0.020	0.030 $^{+0.041}_{-0.023}$	1.054 $^{+0.093}_{-0.081}$
HD 17051	ι Hor	2.13	3.89	3.91	89.5 $^{+144}_{-66.5}$	7.7 $^{+0.18}_{-0.67}$	1.19 \pm 0.07	1.161 \pm 0.017	51.52 $^{+72.96}_{-33.75}$	0.562 $^{+0.162}_{-0.123}$
HD 20630	κ^1 Cet	16.0	15.6	11.1	118. $^{+198}_{-88.9}$	9 \pm 0.5	1.05 \pm 0.06	0.914 \pm 0.014	96.01 $^{+88.30}_{-55.94}$	0.339 $^{+0.043}_{-0.034}$
HD 22049	ϵ Eri	14.6	8.78	5.90	22.4 $^{+34.4}_{-16.3}$	12 \pm 0.5	0.86 \pm 0.05	0.694 \pm 0.014	11.85 $^{+10.25}_{-6.646}$	0.303 $^{+0.025}_{-0.023}$
HD 76151	...	5.98	2.15	0.28	29.2 $^{+39.4}_{-19.8}$	15 \pm 0.5	1.05 \pm 0.06	0.964 \pm 0.018	12.98 $^{+9.933}_{-6.654}$	0.613 $^{+0.087}_{-0.068}$
HD 100180	88 Leo	4.03 $^{+0.53}_{-0.00}$	6.44 $^{+8.68}_{-4.49}$	14 \pm 0.5	1.12 \pm 0.07	1.132 \pm 0.032	6.969 $^{+7.269}_{-3.795}$	0.887 $^{+0.265}_{-0.184}$
HD 101501	61 UMa	11.5	12.0	6.12	29.8 $^{+36.3}_{-19.0}$	17 \pm 0.5	0.97 \pm 0.06	0.855 \pm 0.014	14.71 $^{+10.22}_{-6.992}$	0.542 $^{+0.052}_{-0.046}$
HD 103095	...	0.61 $^{+0.03}_{-0.04}$	0.05 $^{+0.07}_{-0.04}$	31 \pm 0.5	0.60 \pm 0.04	0.641 \pm 0.016	0.008 $^{+0.007}_{-0.005}$	0.933 $^{+0.068}_{-0.062}$
HD 143761	ρ CrB	1.28 $^{+0.46}_{-0.46}$	0.24 $^{+0.32}_{-0.20}$	17 \pm 0.5	1.05 \pm 0.06	1.300 \pm 0.025	0.529 $^{+0.701}_{-0.409}$	0.965 $^{+0.314}_{-0.210}$
HD 146233	18 Sco	1.34	2.01	0.86	0.36 $^{+0.39}_{-0.23}$	22.7 \pm 0.5	1.07 \pm 0.06	1.009 \pm 0.019	0.231 $^{+0.147}_{-0.110}$	0.985 $^{+0.172}_{-0.121}$
HD 166620	...	2.81 $^{+0.95}_{-0.94}$	0.53 $^{+0.58}_{-0.34}$	43 \pm 0.5	0.83 \pm 0.05	0.771 \pm 0.019	0.135 $^{+0.156}_{-0.087}$	1.033 $^{+0.071}_{-0.065}$
HD 185144	σ Dra	5.68	4.82	4.76	4.17 $^{+5.91}_{-3.01}$	27 \pm 0.5	0.86 \pm 0.05	0.769 \pm 0.013	1.232 $^{+0.932}_{-0.666}$	0.762 $^{+0.060}_{-0.052}$
HD 186408	16 Cyg A	0.46 $^{+0.45}_{-0.44}$	1.30 $^{+1.37}_{-0.78}$	20.5 $^{+2.0}_{-1.1}$	1.10 \pm 0.07	1.231 \pm 0.024	0.358 $^{+0.768}_{-0.327}$	1.036 $^{+0.308}_{-0.215}$
HD 186427	16 Cyg B	0.88 $^{+1.04}_{-0.73}$	0.42 $^{+0.46}_{-0.26}$	21.2 $^{+1.8}_{-1.5}$	1.05 \pm 0.06	1.157 \pm 0.019	0.283 $^{+0.708}_{-0.254}$	0.919 $^{+0.246}_{-0.157}$
HD 217014	51 Peg	0.77	0.44	0.65	0.20 $^{+0.27}_{-0.17}$	21.9 \pm 0.4	1.10 \pm 0.07	1.174 \pm 0.023	0.168 $^{+0.125}_{-0.113}$	1.073 $^{+0.290}_{-0.196}$
HD 219134	...	2.39	4.05	1.19	0.31 $^{+0.31}_{-0.16}$	42.2 \pm 0.9	0.80 \pm 0.05	0.724 \pm 0.014	0.073 $^{+0.044}_{-0.028}$	0.892 $^{+0.058}_{-0.057}$

NOTE—A machine-readable version of this table includes additional columns (T_{eff} , $\log g$, $[M/H]$, $v \sin i$, $\log R'_{\text{HK}}$, P_{cyc} , L_X , L_{bol}) that are not displayed here.

There is no single source that includes rotation periods P_{rot} for all of our targets, but the largest uniform compilation comes from the Mount Wilson survey (Baliunas et al. 1996; Simpson et al. 2010). We adopted these values for 12 of our 17 targets, with the rest derived from Zeeman-Doppler imaging (ZDI; Petit et al. 2008; Alvarado-Gómez et al. 2018; Folsom et al. 2018) or asteroseismology (Hall et al. 2021). The uniform properties for the sample are listed in Table 1.

2.2. Magnetic Morphology

For the ten targets with existing ZDI maps, we followed the procedures described by Metcalfe et al. (2024) to derive equivalent polar field strengths for the dipole, quadrupole, and octupole components of the large-scale magnetic field (B_d , B_q , B_o). We adopted these values without revision for 18 Sco (Petit et al. 2008; Metcalfe et al. 2022), 61 UMa (See et al. 2019; Metcalfe et al. 2023), 51 Peg (Metcalfe et al. 2024), as well as ϵ Eri, σ Dra, 107 Psc, and HD 219134 (Jefers et al. 2014; Folsom et al. 2018; Metcalfe et al. 2025). For HD 76151 we analyzed a new ZDI map obtained in 2024 January near its mean activity level (Bellotti et al. 2025), which showed better agreement with the rotation period determined by Baliunas et al. (1996). To provide additional context, we also analyzed ZDI maps for the active stars ι Hor (Alvarado-Gómez et al. 2018) and κ^1 Cet (do Nascimento et al. 2016).

For the seven targets with circular polarization (Stokes V) profiles obtained at a single rotational phase, we made the conservative assumption that all of the field was in the dipole component—maximizing the resulting torque estimate. Fol-

lowing the procedures described by Metcalfe et al. (2022), we modeled each Stokes V profile with an axisymmetric dipole field assuming a fixed stellar inclination. For τ Cet the inclination was fixed from the orientation of its debris disk (Lawler et al. 2014), while for 16 Cyg A and B the inclinations were fixed at the asteroseismic values derived by Hall et al. (2021). For the remaining targets we used the adopted stellar properties ($v \sin i$, P_{rot} , R) to calculate a posterior distribution for the inclination following Bowler et al. (2023), and we adopted the median value. In one case (88 Leo) the observed Stokes V profile was clearly non-axisymmetric, so we modeled it with a tilted dipole following the procedures described by Santos et al. (2025).

2.3. Mass-Loss Rate

We followed the procedures described by Ayres (2025) to obtain a uniform set of X-ray luminosities L_X , and we adopted the empirical relation of Wood (2018) to estimate mass-loss rates \dot{M} from the resulting X-ray surface fluxes F_X . Our approach to determine an X-ray luminosity for each target involved reconciling all of the available measurements from ROSAT, Chandra, and XMM with the adopted stellar properties. Count rates from each of these missions were converted to X-ray fluxes at Earth using an optimization scheme based on a grid of coronal emission-measure models, including a model-based determination of optimum energy conversion factors for each instrument. We adopted the mean from the available X-ray measurements to obtain a representative value of L_X , with the standard deviation serving

as a proxy of the long-term variability from stellar cycles and the systematic differences between the various instruments.

To estimate mass-loss rates we have previously adopted the empirical relation of Wood et al. (2021) for GKM dwarfs, which covers a broader range of F_X and has a shallower dependence $\dot{M} \propto F_X^{0.77 \pm 0.04}$. This is the more conservative choice because it predicts a slower decline in \dot{M} at low F_X near the onset of WMB. However, the scatter in the Wood et al. (2021) relation is large, particularly at high activity levels. By contrast, the scatter in the Wood (2018) relation for GK dwarfs is roughly plus or minus a factor of two, which is consistent with the systematic noise floor estimated by Wood et al. (2005). Having previously demonstrated that our conclusions do not depend on this choice, we adopted the steeper relation $\dot{M} \propto F_X^{1.29 \pm 0.16}$ from Wood (2018). We combined the quoted factor of two systematic error in quadrature with the errors on L_X , R , and the power law exponent to determine the total uncertainty in our estimated mass-loss rates.

3. MODELING

The ultimate goal of our analysis is to determine empirically how the wind braking torque changes with the Rossby number across the transition to WMB. In this section we define a homogeneous Ro scale from detailed evolutionary modeling (§3.1) and we update our estimates of the wind braking torque (§3.2), drawing from the uniform observational inputs described in Section 2.

3.1. Rossby Scale

We defined a uniform Ro scale using the model grids described by Metcalfe et al. (2025), extended to cover the range of masses, metallicities, and evolutionary states in our sample. We inferred convective overturn timescales one pressure scale height above the convective boundary using a fitting method identical to that in Metcalfe et al. (2025) with one difference: we did not utilize P_{rot} as a constraint for the fit, instead using only the observational constraints on T_{eff} , R , and $[M/H]$. This makes our analysis independent of the choice of rotational evolution model at the expense of slightly larger uncertainties in the inferred convective overturn timescales, τ_c . We define the Rossby number as $\text{Ro} \equiv P_{\text{rot}}/\tau_c$ using the measured rotation period and the model-inferred overturn timescale with their respective uncertainties.

The largest Rossby numbers in our sample are less than 1.1 Ro_{\odot} , in line with expectations from the WMB scenario, despite the fact that the Ro scale defined here is agnostic to the rotational evolution model. The WMB hypothesis predicts very mild evolution of Ro after the onset of weakened braking, due to an increasing moment of inertia under approximate conservation of angular momentum. Using the braking models described by Metcalfe et al. (2025), a solar model with WMB has a main-sequence turnoff (core H frac-

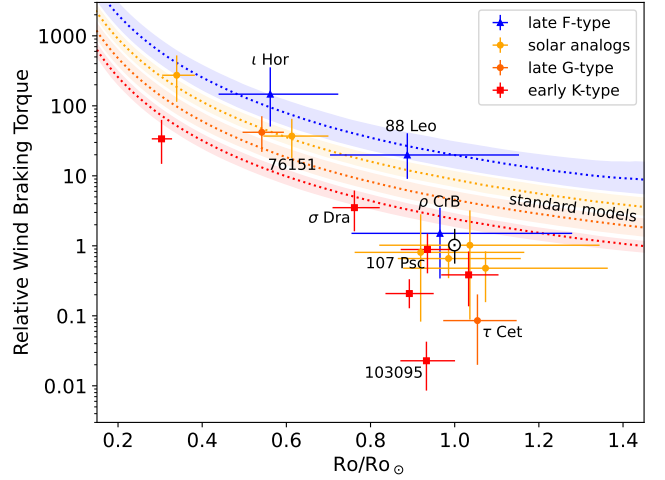


Figure 1. Relative wind braking torque as a function of Rossby number normalized to the solar value. Points are grouped by spectral type as shown in the legend. Standard spin-down models for the mean stellar properties within each spectral type are shown for reference. The solar point \odot is from Finley et al. (2018).

tion < 0.0001) at $\text{Ro} \sim 1.1 \text{ Ro}_{\odot}$, while standard spin-down models would predict $\text{Ro} \sim 1.8 \text{ Ro}_{\odot}$ at the turnoff.

The large uncertainties on Ro, for the F-type stars in particular, are a reflection of the basic behavior of τ_c as a function of surface temperature. F-type stars have rapidly thinning convection zones with increasing surface temperature (Kraft 1967), and thus rapidly decreasing τ_c . Typical observational uncertainties on T_{eff} therefore translate into larger uncertainties on Ro compared to the cooler stars.

3.2. Wind Braking Torque

Adopting the uniform observational inputs described in Section 2, we updated the torque estimates for our sample using the wind braking prescription of Finley & Matt (2018)¹. The observational inputs for each star are listed in Table 1, including the large-scale magnetic field components from ZDI maps or Stokes V snapshots, mass-loss rates from the Wood (2018) empirical relation, rotation periods primarily from the Mount Wilson survey (Baliunas et al. 1996), stellar masses from the Torres et al. (2010) empirical relation, and stellar radii from SED fitting. Uncertainties were determined by simultaneously shifting all of the inputs to their $\pm 1\sigma$ values to minimize or maximize the torque. The results are illustrated in Figure 1, with the wind braking torque plotted against the Ro scale described in Section 3.1. Our standard spin-down models are shown for the mean stellar properties within each spectral type, revealing the mass-dependence of the absolute torque and emphasizing deviations from the predicted evolution as Ro approaches and exceeds the solar value.

¹ <https://github.com/travismetcalfe/FinleyMatt2018>

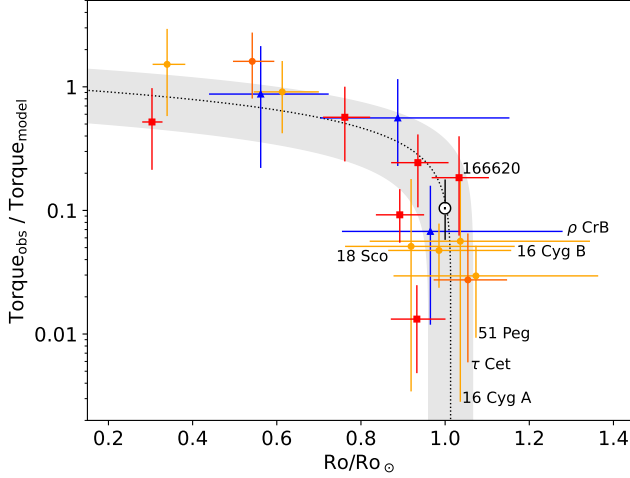


Figure 2. Ratio of the observationally estimated and model wind braking torque as a function of Rossby number normalized to the solar value. The dotted line illustrates the fit described in Section 4, and the 95% confidence interval is shown as a gray shaded region. Flat activity stars and other targets discussed in the text are labeled.

The results are qualitatively similar to our previously published analyses, showing an abrupt change in the estimated wind braking torque as the Rossby number approaches a critical value. The inclusion of ι Hor to provide additional context for our observations of late F-type stars reveals that 88 Leo already exhibits some evidence of WMB, while ρ CrB remains clearly in the WMB regime with a torque that is 15 times weaker than a standard spin-down model. The adoption of a different rotation period for HD 76151 shifts it well below the onset of WMB, while the more slowly rotating solar analogs have torques that are 20–30 times weaker than standard models. The results for late G-type stars do not strongly constrain the onset of WMB, but the estimated torque for metal-poor τ Cet is nearly a factor of 40 below a standard model. The K-type star σ Dra appears to be approaching the WMB regime, while the more slowly rotating K dwarfs have torques that are 4–70 times weaker than expected from standard models—from the transitional star 107 Psc to the extremely metal-poor star HD 103095.

In Figure 2 we show the ratio of the observationally estimated and model torques for each of the stars in our sample, normalized to place the observations and models on the same scale. This representation allows us to determine the magnitude of the deviation of observations from our standard spin-down models, and assess whether the onset of WMB is instantaneous or gradual. By construction, the active targets at low Ro are scattered around unity, indicating agreement with standard spin-down models. By contrast, the targets at higher Ro exhibit an abrupt decrease of nearly two orders of magnitude as Ro becomes comparable to the solar value. In the following section, we discuss our motivation for fitting the specific functional form that is shown in Figure 2.

4. DISCUSSION

Our uniform analysis of a sample of targets spanning the transition to WMB motivates a paradigm shift in our interpretation of the results. For each of the evolutionary sequences that we have previously analyzed, we sought to identify a critical Rossby number (Ro_{crit}) beyond which magnetic braking effectively ceased. As we gradually expanded the sample, we attempted to trace the onset of WMB back to its root causes—from its influence on stellar rotation periods, to a hypothesized shift in magnetic morphology, and ultimately to the evolution of the global stellar dynamo. In an effort to understand solar cycle variability, Cameron & Schüssler (2017) proposed that the global solar dynamo can be considered a “weakly nonlinear system in the vicinity of a supercritical Hopf bifurcation.” Within this framework, the control parameter is the dynamo number $D \sim Ro^{-2}$ (Durney & Latour 1978), and the system exhibits a periodic solution as long as D exceeds a critical value. Below the critical value of D (when Ro is sufficiently large), the global dynamo is not excited. Generically, this suggests that the solar dynamo should be mildly supercritical (Wavhal et al. 2025) and that related observables should vary with $N\sqrt{Ro_{crit} - Ro}$, where N is a normalization constant. The adoption of this functional form suggests that the onset of WMB occurs gradually as Ro approaches (rather than exceeds) Ro_{crit} . This appears to be supported by the data in Figure 2, where N is primarily constrained by the most active stars in the sample and Ro_{crit} is largely determined by stars with $Ro \sim Ro_{\odot}$.

The two axes of Figure 2 are not entirely independent, so we used an iterative strategy to estimate the values of N and Ro_{crit} . We initially set the value of $N = 0.329$ from the mean of the seven most active stars, which agree with our standard spin-down models. We then used the stars with $Ro > 0.7$ to determine the optimal value of $Ro_{crit} = 1.014 \pm 0.026 Ro_{\odot}$, considering only the horizontal uncertainties. Finally, we fixed Ro_{crit} at its optimal value and reoptimized the value of $N = 0.354 \pm 0.077$, considering only the vertical uncertainties. The optimal value of N was also within this range when fixing Ro_{crit} at its $\pm 1\sigma$ limits. Although this specific solution may not be unique, it is representative of the families of solutions that we identified using a variety of fitting strategies. The dotted line in Figure 2 illustrates our iterative fit, with the 95% confidence interval shown as a gray shaded region. As expected from the suggestion of Cameron & Schüssler (2017), Ro_{crit} is slightly above the solar value and establishes an approximate dividing line between stars with activity cycles and those with flat activity. Aside from the Sun, the cycling star with the highest value of Ro is 18 Sco, while the stars above Ro_{crit} all show flat activity. The flat activity stars ρ CrB and 16 Cyg B have $Ro < Ro_{crit}$, but the uncertainties extend well above Ro_{crit} . The magnetic grand minimum star HD 166620 has $Ro > Ro_{crit}$, but the uncertainty

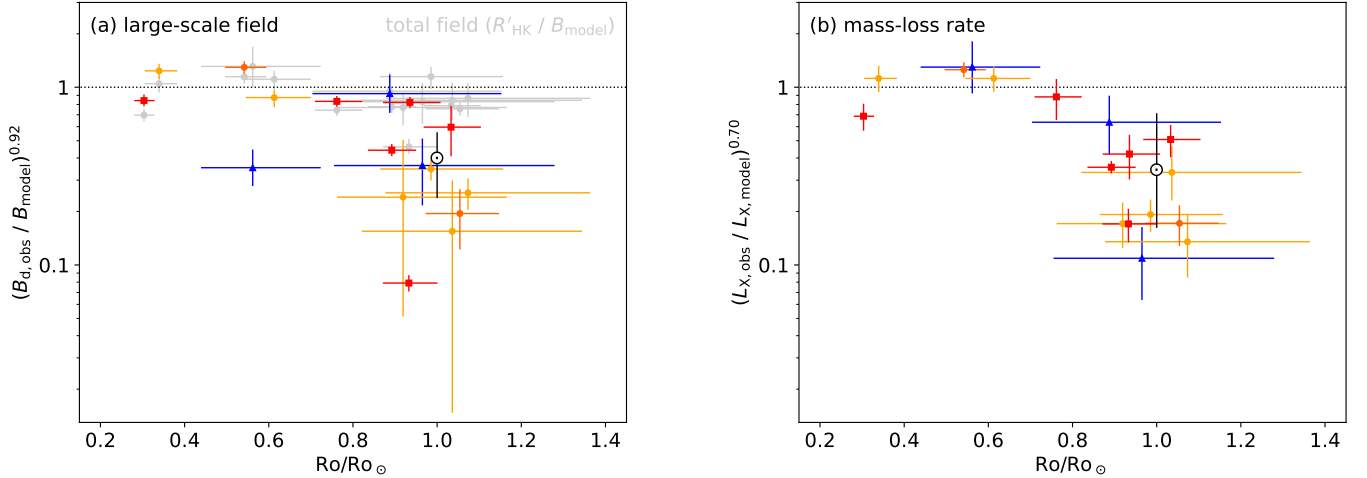


Figure 3. Ratio of observations and model predictions as a function of Rossby number normalized to the solar value. Each ratio has been raised to a power that reflects its relative contribution to the change in wind braking torque and normalized so that unity represents agreement. (a) Dipole magnetic field strength as a proxy for the large-scale field, and (b) X-ray luminosity, reflecting changes in the stellar mass-loss rate. The solar dipole field strength is from [Finley et al. \(2018\)](#), while the X-ray luminosity over a complete solar cycle is from [Judge et al. \(2003\)](#).

extends slightly below Ro_{crit} where simulations suggest that grand minima occur ([Vashishth et al. 2023](#)).

The deviation of the estimated wind braking torque from the predictions of standard models can be traced to unexpected changes in both the large-scale magnetic field strength and the X-ray luminosity. Our standard models predict $B \sim P_{phot}^{1/2}/Ro$ (where P_{phot} is the photospheric pressure), and $L_X \sim L_{bol}/Ro^2$ ([van Saders & Pinsonneault 2013](#); [Saunders et al. 2024](#)). In Figure 3 we show the ratio of the observations and the model predictions for our sample, raised to powers that reflect their relative contributions to the wind braking torque and normalized so that unity represents agreement. We see deviations of up to an order of magnitude in each of these observables as Ro approaches Ro_{crit} . The low blue point on the left side of Figure 3a is ι Hor, which is the only star in our sample with a wind braking torque that is not in the dipole-dominated regime of [Finley & Matt \(2018\)](#). Aside from this point, the trend with Ro resembles the pattern seen in Figure 2. By contrast, the normalized ratios of R'_{HK} to B_{model} (gray points) are scattered around unity across the full range of Ro . This suggests that while our standard model correctly reproduces the evolution of the total magnetic field strength, it fails to predict the observed changes in the large-scale field (represented by B_d) for stars near Ro_{crit} . As we have noted before, the solar R'_{HK} is dominated by a $\langle B \rangle \sim 170$ G contribution from the unstructured quiet Sun, which dwarfs the ~ 1 G dipole component of the field inferred from ZDI maps ([Metcalfe et al. 2019](#)). The dipole field can disappear entirely with negligible impact on R'_{HK} , but with severe consequences for the wind braking torque.

The change in the observed X-ray luminosity shown in Figure 3b may represent a decrease in the mass-loss rate that is captured by the empirical relation of [Wood \(2018\)](#).

Three of the targets in our sample (ϵ Eri, HD 219134, τ Cet) have direct inferences of the mass-loss rate from $Ly\alpha$ measurements ($30, 0.5, 0.1 \dot{M}_{\odot}$), which broadly agree with the values predicted from their X-ray surface fluxes ($22.4^{+34.4}_{-16.3}, 0.31^{+0.31}_{-0.16}, 0.10^{+0.13}_{-0.08} \dot{M}_{\odot}$). This suggests that the observed decrease in wind braking torque is not an artifact of the empirical relation used to scale the X-ray luminosity. Instead, it may reflect a genuine decrease in the mass-loss rate. Furthermore, the observed changes in B_d and L_X can both be understood as consequences of a near-critical dynamo and the resulting decrease in Poynting flux. As a star approaches Ro_{crit} , its internal dynamo becomes less efficient. This leads to a weaker large-scale magnetic field and a subsequent decrease in the outward-propagating Poynting flux, or magnetic energy flow. The resulting reduction in Poynting flux directly affects two key processes: it provides less energy for coronal heating, which lowers the X-ray luminosity, and it reduces the magnetic pressure that accelerates the stellar wind, which in turn reduces the mass-loss rate.

In hindsight, a rotational threshold for the excitation of a global stellar dynamo is understandable considering the role of the Coriolis force, which imposes a tilt on emerging bipolar magnetic regions and imprints organizing flows on the convective patterns ([Roland-Batty et al. 2025](#)). A smaller Joy’s law tilt yields enhanced cancellation before the weaker differential rotation can separate the leading and trailing polarities. Inefficient meridional circulation then transports less residual magnetic flux to the polar regions, stunting the dipole field for the subsequent cycle. In addition, weaker differential rotation operating on a weaker dipole field is less efficient at winding up the poloidal field to produce toroidal flux tubes near the base of the convection zone, inhibiting flux emergence and leading to a downward spiral

of the dipole field strength. The lower mass-loss rate appears to be a consequence of the diminishing magnetic energy that is available from the global dynamo. The increase in high-order magnetic complexity might also throttle the stellar wind, which escapes along open magnetic field lines (Garraffo et al. 2015; Shoda et al. 2023).

The Rossby number plays a central role in theoretical models of stellar winds, and it has been implicitly invoked in empirical studies. Our results strongly reinforce this hypothesis. Across a wide range of spectral types, Ro-scaled models predict reliable torques for the active stars. For less active stars, a dramatic decrease in torques is seen. WMB emerges at a consistent Ro across a wide range of stellar metallicities and convective overturn timescales. At higher Ro, we see unexpected decreases in both large-scale magnetic field strength and coronal heating. We caution that our observations do not reach the fully convective domain. We therefore cannot draw conclusions about the similarity of the dynamo mechanism in stars with radiative cores versus fully convective stars.

Future observations from ESA’s PLATO mission could help expand the current sample of bright stars with measured rotation periods and stellar properties from asteroseismology (Rauer et al. 2025). Although a specific target list has not yet been released, the footprint of the first $49^\circ \times 49^\circ$ field contains more than 100 bright stars with measured chromospheric activity levels (Henry et al. 1996). About half of these potential targets are in the low-activity range ($\log R'_{\text{HK}} \lesssim -4.9$) where

the effects of WMB start to become apparent, and dozens are also bright enough for spectropolarimetry to be feasible with HARPSpol. The Galactic longitude of the field is well within the German half of the eROSITA all-sky survey (eRASS; Predehl et al. 2021), so X-ray surface fluxes might be available from eRASS DR2 (mid-2026) or ultimately DR3 (late 2028). With patience and some luck, the current sample of bright solar-type stars that probe the WMB regime will be expanded substantially over the coming years, providing a broader context for our understanding of magnetic stellar evolution during the second half of main-sequence lifetimes.

The authors would like to thank Robert Cameron for discussions that substantially informed our interpretation of these observations, as well as Stefano Bellotti and Gaitee Hussain for sharing details about their published ZDI maps. Early support for this project came from the Max Planck Institute for Solar System Research (2018) and the Vanderbilt Initiative in Data-intensive Astrophysics (2021). T.S.M. and J.v.S. acknowledge support from NSF grants AST-2205919 and AST-2205888, respectively. O.K. acknowledges support from the Swedish Research Council (grant agreement 2023-03667) and from the Swedish National Space Agency. A.J.F. and V.S. received funding from the European Research Council (ERC) under the European Union’s Horizon 2020 research and innovation programme (grant agreements 810218 WHOLESUN and 804752 CartographY, respectively).

REFERENCES

- Alvarado-Gómez, J. D., Hussain, G. A. J., Drake, J. J., et al. 2018, *MNRAS*, **473**, 4326
- Ayres, T. 2025, *AJ*, **169**, 281
- Baliunas, S., Sokoloff, D., & Soon, W. 1996, *ApJL*, **457**, L99
- Barnes, S. A. 2007, *ApJ*, **669**, 1167
- Bellotti, S., Petit, P., Jeffers, S. V., et al. 2025, *A&A*, **693**, A269
- Borucki, W. J., Koch, D., Basri, G., et al. 2010, *Science*, **327**, 977
- Bowler, B. P., Tran, Q. H., Zhang, Z., et al. 2023, *AJ*, **165**, 164
- Brewer, J. M., Fischer, D. A., Valenti, J. A., & Piskunov, N. 2016, *ApJS*, **225**, 32
- Cameron, R. H., & Schüssler, M. 2017, *ApJ*, **843**, 111
- Charbonneau, P., & MacGregor, K. B. 1993, *ApJ*, **417**, 762
- do Nascimento, Jr., J. D., Vidotto, A. A., Petit, P., et al. 2016, *ApJL*, **820**, L15
- Durney, B. R., & Latour, J. 1978, *GApFD*, **9**, 241
- Finley, A. J., & Matt, S. P. 2018, *ApJ*, **854**, 78
- Finley, A. J., Matt, S. P., & See, V. 2018, *ApJ*, **864**, 125
- Folsom, C. P., Fossati, L., Wood, B. E., et al. 2018, *MNRAS*, **481**, 5286
- Gaia Collaboration, Brown, A. G. A., Vallenari, A., et al. 2021, *A&A*, **649**, A1
- Gallet, F., & Bouvier, J. 2013, *A&A*, **556**, A36
- Garraffo, C., Drake, J. J., & Cohen, O. 2015, *ApJ*, **813**, 40
- Garraffo, C., Drake, J. J., Dotter, A., et al. 2018, *ApJ*, **862**, 90
- Hall, O. J., Davies, G. R., van Saders, J., et al. 2021, *Nature Astronomy*, **5**, 707
- Henry, T. J., Soderblom, D. R., Donahue, R. A., & Baliunas, S. L. 1996, *AJ*, **111**, 439
- Jeffers, S. V., Petit, P., Marsden, S. C., et al. 2014, *A&A*, **569**, A79
- Judge, P. G., Solomon, S. C., & Ayres, T. R. 2003, *ApJ*, **593**, 534
- Koenigl, A. 1991, *ApJL*, **370**, L39
- Kraft, R. P. 1967, *ApJ*, **150**, 551
- Krishnamurthi, A., Pinsonneault, M. H., Barnes, S., & Sofia, S. 1997, *ApJ*, **480**, 303
- Lawler, S. M., Di Francesco, J., Kennedy, G. M., et al. 2014, *MNRAS*, **444**, 2665
- MacGregor, K. B., & Brenner, M. 1991, *ApJ*, **376**, 204
- Matt, S. P., MacGregor, K. B., Pinsonneault, M. H., & Greene, T. P. 2012, *ApJL*, **754**, L26
- McQuillan, A., Mazeh, T., & Aigrain, S. 2014, *ApJS*, **211**, 24
- Mermilliod, J. C. 2006, *yCat*, **II/168**

- Metcalfe, T. S., Kochukhov, O., Ilyin, I. V., et al. 2019, [ApJL](#), **887**, L38
- Metcalfe, T. S., van Saders, J. L., Basu, S., et al. 2021, [ApJ](#), **921**, 122
- Metcalfe, T. S., Finley, A. J., Kochukhov, O., et al. 2022, [ApJL](#), **933**, L17
- Metcalfe, T. S., Strassmeier, K. G., Ilyin, I. V., et al. 2023, [ApJL](#), **948**, L6
- . 2024, [ApJL](#), **960**, L6
- Metcalfe, T. S., Petit, P., van Saders, J. L., et al. 2025, [ApJ](#), **986**, 120
- Paunzen, E. 2015, [A&A](#), **580**, A23
- Petit, P., Dintrans, B., Solanki, S. K., et al. 2008, [MNRAS](#), **388**, 80
- Pinsonneault, M. 1997, [ARA&A](#), **35**, 557
- Pinsonneault, M. H., Kawaler, S. D., & Demarque, P. 1990, [ApJS](#), **74**, 501
- Pinsonneault, M. H., Kawaler, S. D., Sofia, S., & Demarque, P. 1989, [ApJ](#), **338**, 424
- Predehl, P., Andritschke, R., Arefiev, V., et al. 2021, [A&A](#), **647**, A1
- Radick, R. R., Thompson, D. T., Lockwood, G. W., Duncan, D. K., & Baggett, W. E. 1987, [ApJ](#), **321**, 459
- Rauer, H., Aerts, C., Cabrera, J., et al. 2025, [Experimental Astronomy](#), **59**, 26
- Reiners, A., & Mohanty, S. 2012, [ApJ](#), **746**, 43
- Roland-Batty, W., Schunker, H., Cameron, R. H., et al. 2025, [A&A](#), **700**, A28
- Santos, A. R. G., Metcalfe, T. S., Kochukhov, O., et al. 2025, [A&A](#), **698**, L23
- Saunders, N., van Saders, J. L., Lyttle, A. J., et al. 2024, [ApJ](#), **962**, 138
- See, V., Matt, S. P., Finley, A. J., et al. 2019, [ApJ](#), **886**, 120
- Shoda, M., Cranmer, S. R., & Toriumi, S. 2023, [ApJ](#), **957**, 71
- Shu, F. H., Johnstone, D., & Hollenbach, D. 1993, [Icarus](#), **106**, 92
- Simpson, E. K., Baliunas, S. L., Henry, G. W., & Watson, C. A. 2010, [MNRAS](#), **408**, 1666
- Skumanich, A. 1972, [ApJ](#), **171**, 565
- Soderblom, D. R., Jones, B. F., & Walker, M. F. 1983, [ApJL](#), **274**, L37
- Spada, F., & Lanzafame, A. C. 2020, [A&A](#), **636**, A76
- Stassun, K. G., Collins, K. A., & Gaudi, B. S. 2017, [AJ](#), **153**, 136
- Stassun, K. G., Corsaro, E., Pepper, J. A., & Gaudi, B. S. 2018, [AJ](#), **155**, 22
- Stassun, K. G., & Torres, G. 2016, [ApJL](#), **831**, L6
- Stauffer, J. R., & Hartmann, L. W. 1987, [ApJ](#), **318**, 337
- Torres, G., Andersen, J., & Giménez, A. 2010, [A&A Rv](#), **18**, 67
- Valenti, J. A., & Fischer, D. A. 2005, [ApJS](#), **159**, 141
- van Saders, J. L., Ceillier, T., Metcalfe, T. S., et al. 2016, [Nature](#), **529**, 181
- van Saders, J. L., & Pinsonneault, M. H. 2013, [ApJ](#), **776**, 67
- van Saders, J. L., Pinsonneault, M. H., & Barbieri, M. 2019, [ApJ](#), **872**, 128
- Vashishth, V., Karak, B. B., & Kitchatinov, L. 2023, [MNRAS](#), **522**, 2601
- Wavhal, S., Kumar, P., & Karak, B. B. 2025, [SoPh](#), **300**, 21
- Weber, E. J., & Davis, Leverett, J. 1967, [ApJ](#), **148**, 217
- Wood, B. E. 2018, [JPhCS](#), **1100**, 012028
- Wood, B. E., Müller, H. R., Zank, G. P., Linsky, J. L., & Redfield, S. 2005, [ApJL](#), **628**, L143
- Wood, B. E., Müller, H.-R., Redfield, S., et al. 2021, [ApJ](#), **915**, 37